ACS NANO

www.acsnano.org

ARTICLE

Te-Vacancy-Induced Surface Collapse and Reconstruction in Antiferromagnetic Topological Insulator $MnBi_2Te_4$

Fuchen Hou,[#] Qiushi Yao,[#] Chun-Sheng Zhou, Xiao-Ming Ma, Mengjiao Han, Yu-Jie Hao, Xuefeng Wu, Yu Zhang, Hongyi Sun, Chang Liu, Yue Zhao,* Qihang Liu,* and Junhao Lin*

Cite This: *ACS Nano* 2020, 14, 11262−11272

Read Online

ACCESS | Metrics & More | Article Recommendations | Supporting Information

ABSTRACT: **$MnBi_2Te_4$ is an antiferromagnetic topological insulator that has stimulated intense interest due to its exotic quantum phenomena and promising device applications. The surface structure is a determinant factor to understand the magnetic and topological behavior of $MnBi_2Te_4$, yet its precise atomic structure remains elusive. Here we discovered a surface collapse and reconstruction of few-layer $MnBi_2Te_4$ exfoliated under delicate protection. Instead of the ideal septuple-layer structure in the bulk, the collapsed surface is shown to reconstruct as a Mn-doped Bi_2Te_3 quintuple layer and a Mn_xBi_yTe double layer with a clear van der Waals gap in between. Combined with first-principles calculations, such surface collapse is attributed to the abundant intrinsic Mn−Bi antisite defects and the tellurium vacancy in the exfoliated surface, which is further supported by *in situ* annealing and electron irradiation experiments. Our results shed light on the understanding of the intricate surface-bulk correspondence of $MnBi_2Te_4$ and provide an insightful perspective on the surface-related quantum measurements in $MnBi_2Te_4$ few-layer devices.**

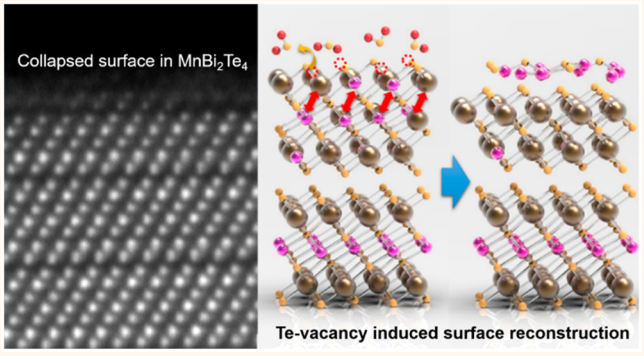

KEYWORDS: *surface reconstruction, $MnBi_2Te_4$, magnetic topological insulator, antisite defects, tellurium vacancy, in situ surface dynamics*

Magnetic topological quantum materials have stimulated intense research interest due to the interplay between magnetism and topology that results in an emerging quantum phenomenon.[1−4] Examples include the quantum anomalous Hall effect (QAHE),[3−5] Weyl semimetallic states,[6,7] topological axion states,[8] Majorana fermions,[2,9] and so on, enabling potential applications in dissipationless electronic and quantum computing.[10] In the early research, a magnetic topological insulator (TI) was achieved by magnetically doping a TI thin film to study the QAHE.[3−5] However, the random distribution of magnetic dopants introduces impurity scattering together with the ferromagnetic ordering, limiting the temperature for the realization of the QAHE. Very recently, the tetradymite-type $MnBi_2Te_4$ compound was discovered as an intrinsic antiferromagnetic (AFM) TI in the *A*-type AFM ground state with out-of-plane magnetic moments.[11−19] Although the existence of long-range magnetic order explicitly breaks the time-reversal symmetry, which is nevertheless preserved in conventional Z_2 TI,[1,2] another type of Z_2 invariant can be defined in $MnBi_2Te_4$ as long as a combined symmetry between the time reversal and the fractional translation is preserved.[11,20,21] As a result, $MnBi_2Te_4$ provides an ideal platform for magnetic TI to realize the QAHE, the axion insulator state,[15,17,22] and so on.

On the contrary, there are still discrepancies between theoretical expectations and experimental facts in $MnBi_2Te_4$. For instance, theoretical predictions and some experimental observations declared a sizable magnetic gap at the surface of bulk $MnBi_2Te_4$,[11−15] whereas a recent report shows an unambiguously gapless Dirac cone at the (00*l*) surface of $MnBi_2Te_4$ crystal by using the high-resolution angle-resolved photoemission spectroscopy (ARPES).[16,23,24] Such inconsistency implies that the surface structure is a key factor requiring precise measurements, which may affect many of the corresponding magnetic and topological behaviors in $MnBi_2Te_4$, such as the QAHE in odd layers and the zero

Received: April 14, 2020
Accepted: August 19, 2020
Published: August 19, 2020

https://dx.doi.org/10.1021/acsnano.0c03149
ACS Nano 2020, 14, 11262−11272

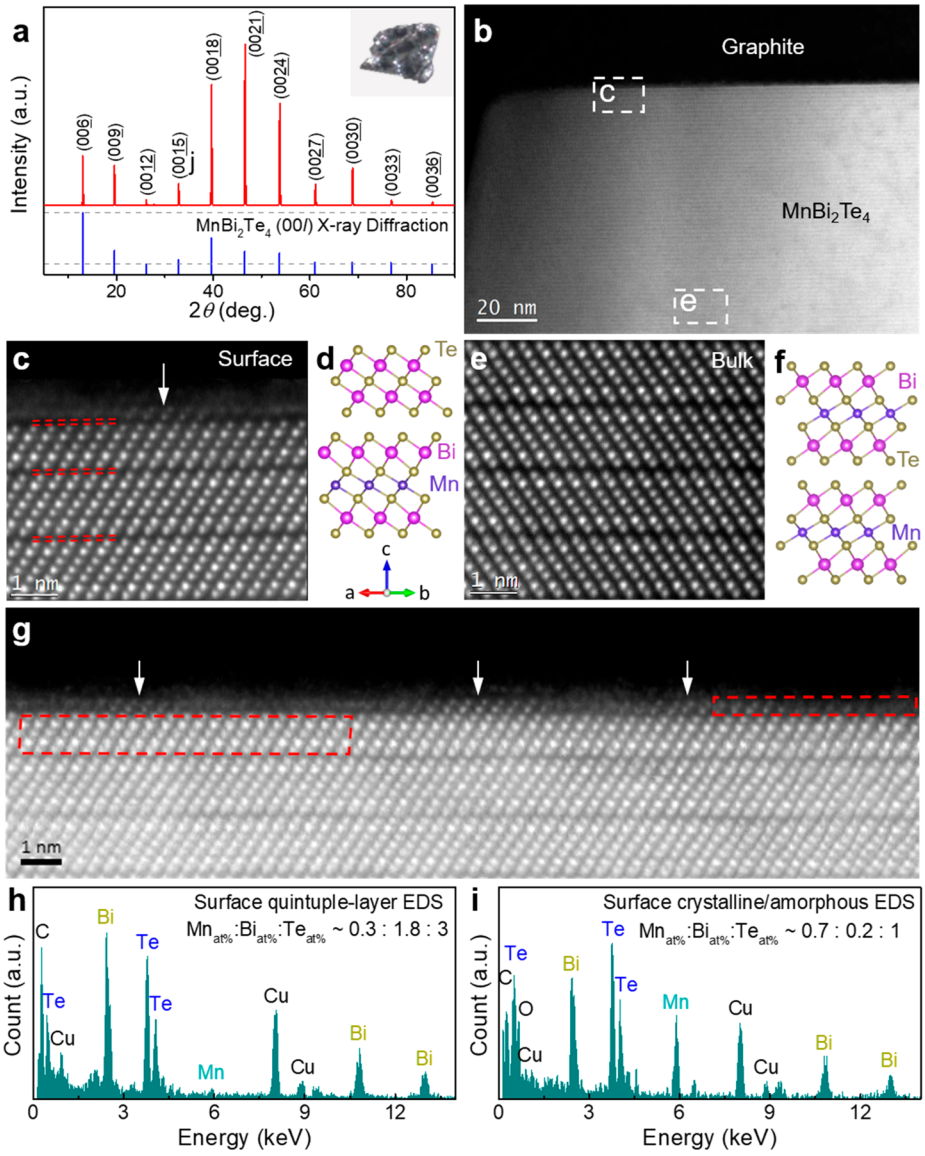

Figure 1. Atomic characterizations of the $MnBi_2Te_4$ surface structure. (a) X-ray diffraction (XRD) pattern (red) and the referenced (00*l*) peaks (blue) from standard PDF file of the parent single $MnBi_2Te_4$ crystal. (b) Large-scale high-angle annular dark-field scanning transmission electron microscopy (HAADF-STEM) image of the cross section of the layered $MnBi_2Te_4$ crystal viewed along the [110] direction, with the overlaid graphite as surface protection. (c–e) Zoom-in atomic-resolution HAADF-STEM images of the surface and bulk highlighted in panel b, respectively. A quintuple layer (QL) with a double-layer (DL) crystalline/amorphous structure, instead of the ideal septuple-layer (SL) $MnBi_2Te_4$, is seen at the surface. The arrows highlight the crystalline DL islands on the surface. (d,f) Corresponding atomic models from the images, respectively. (g) Large-scale atomic structure of the $MnBi_2Te_4$ surface showing the omnipresent crystalline DL islands indicated by arrows. (h,i) Corresponding energy-dispersive spectrum (EDS) maps for the surface QL and DL crystalline/amorphous structures, respectively. Cu and C come from the grid and substrate.

Hall plateau as an indicator of the axion state in even layers.[11,17,18] Apparently, most of the previous results consider the surface structure using the ideal septuple-layer (SL) $MnBi_2Te_4$ lattice,[11−19] which, on the contrary, lacks direct proof to connect the bridge between theory and experiments.

Because the surface-bulk correspondence is the kernel of the topological properties, in this Article, we systematically studied the atomic structure of the surface in $MnBi_2Te_4$ few-layer devices with intended surface protection. Using cross-sectional scanning transmission electron microscopy (STEM) imaging, atomic electron energy loss spectroscopy (EELS), and energy-dispersive spectroscopy (EDS), we unambiguously determined the surface of few-layer $MnBi_2Te_4$ to be a Mn-doped Bi_2Te_3 quintuple layer (QL) decorated with a crystalline/amorphous Mn_xBi_yTe double layer (DL) rather than the ideal SL-layered structure; that is, a surface collapse and reconstruction occurred during the mechanical exfoliation. Such surface collapse is highly reproducible in all samples we measured. We further discovered that Bi−Mn antisite defects were omnipresent in bulk $MnBi_2Te_4$. Combining the density functional theory (DFT) calculations, we unveiled the origin of the surface collapse in few-layer $MnBi_2Te_4$ to be a result of the synergistic interaction between the Bi−Mn antisite defects and the surface tellurium vacancies. Our result shows that such defects are inevitable, even in an inert gas environment, due to trace oxygen, which makes the as-observed reconstructed surface preferential in the energy landscape. Similar surface collapse and reconstruction can be reproduced by heating the

https://dx.doi.org/10.1021/acsnano.0c03149
ACS Nano 2020, 14, 11262−11272

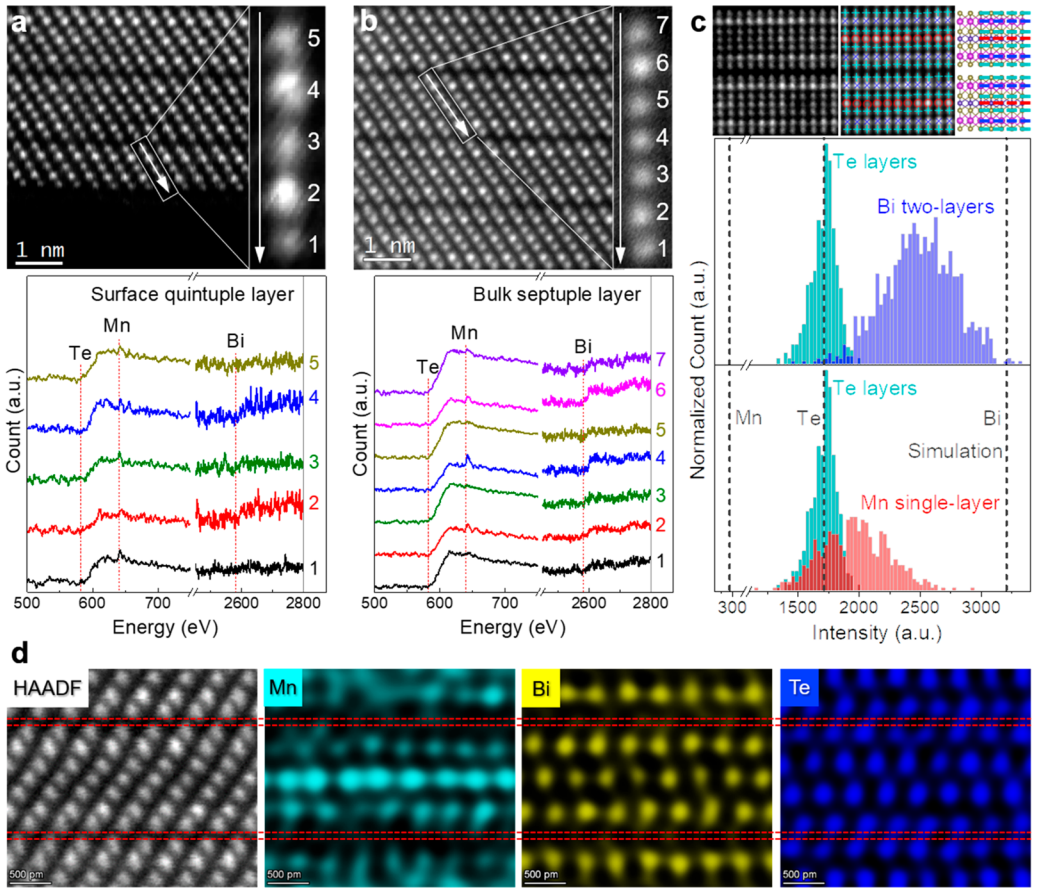

Figure 2. Chemical analysis of the exchange Mn−Bi defects at the surface and bulk. (a,b) Atomic-resolution cross-sectional HAADF images of the single-crystal $MnBi_2Te_4$, with the arrow indicating the position and direction of the electron energy loss spectrometry (EELS) linescan acquisition. The corresponding background-subtracted atom-by-atom EELS data for the (a) surface QL and (b) bulk SL are shown below. The numbers mark the different atomic columns corresponding to the labeled EELS data. The onset energies of Te ($M_{4,5}$ edge at 572 eV), Mn ($L_{2,3}$ edge at 640 eV), and Bi ($M_{4,5}$ edge at 2580 eV) are highlighted by dashed lines as a guide to the eye. (c) Histogram of the intensity distribution mapped from the Te (cyanine), Bi (blue), and Mn (red) atomic columns in bulk $MnBi_2Te_4$, respectively. The HAADF image shows the location of different atomic columns marked by corresponding colors, viewed from the [110] direction. The dark-gray dashed lines represent the normalized intensities of Te, Mn, and Bi columns from the simulation without any Mn−Bi exchange defect. (d) Atomic-resolution HAADF image of the SL structure in $MnBi_2Te_4$ with corresponding EDS mapping for individual elements of Mn, Bi, and Te. The red dashed lines highlight an individual SL.

intact SL surface exfoliated in an ultrahigh vacuum (UHV) and probing by atomic scanning tunneling microscopy (STM) and by electron irradiation in STEM, which simultaneously monitor the dynamical surface collapse and reconstruction process atom-by-atom. These experiments further verified that the surface collapse and reconstruction that occurred in a well-controlled inert gas environment were indeed induced by the surface Te vacancy. Our findings of the vacancy-induced surface collapse and reconstruction in exfoliated $MnBi_2Te_4$ under a well-controlled inert gas environment not only shed light on the fabrication of $MnBi_2Te_4$ few-layer devices but also bring valuable insights into understanding the discrepancies and controversial arguments from many laboratories that are dedicated to $MnBi_2Te_4$ research, such as the discrepancies in the surface electronic structure in previous investigations.[11−16,23,24]

RESULTS AND DISCUSSION

Atomic Structure of the Collapsed Surface in Exfoliated $MnBi_2Te_4$ Few-Layer Devices. The $MnBi_2Te_4$ single crystal is a member of the van der Waals (VDW) layered materials. A single VDW layer of $MnBi_2Te_4$ consists of alternating Bi−Mn−Bi layer intercalated by Te, forming an SL structure. Its antiferromagnetism originates from the middle Mn cations with a superexchanged interlayer interaction between adjacent Mn layers. Figure 1a shows the X-ray diffraction (XRD) measurement of the parent $MnBi_2Te_4$ crystal with sharp and intense peaks that follow the (00l), $l = 3n$, diffraction rule, which quantitatively agree with those in the standard PDF files. In addition, the X-ray photoelectron spectroscopy (XPS) characterization of the $MnBi_2Te_4$ single crystal reveals the core-level peaks of Mn 2p, Bi 4f, and Te 3d (Figure S1) without any impurity signal from other crystalline phases and elements, indicating the high quality of the parent single crystal. The fresh cleaved surface of the $MnBi_2Te_4$ crystal was initially investigated by high-resolution atomic force microscopy (AFM) operated in the same inert gas environment. A rough surface was seen with steps ranging from 2 to 6 Å (one to three atomic layers) (Figure S2), suggesting a possible disordered surface structure. We then performed a cross-section study to obtain atomic information on the surface. The surface was intentionally protected by graphite, which merely serves as a protective layer on the $MnBi_2Te_4$ surface, ensuring minimum surface degradation during cross-

https://dx.doi.org/10.1021/acsnano.0c03149
ACS Nano 2020, 14, 11262−11272

section sample fabrication. (See the Materials and Methods for more details.)

Figure 1b shows a low-magnified high-angle annular dark-field (HAADF) STEM image of the as-prepared $MnBi_2Te_4$ few-layer cross-section, taken from the [110] direction. The graphite appears in dark contrast due to its relative light atomic weight in the STEM image. Zoom-in images with the atomic resolution of the surface and bulk are exhibited in Figure 1c,e, respectively. A comparison of the two readily shows an apparent deviation of the surface structure: It is a five-atom layer instead of seven, similar to the atomic structure of TI Bi_2Te_3 (Te−Bi−Te−Bi−Te) viewed along the *c* axis, known as the QL structure. (The atomic model is shown in Figure 1d.) In contrast, the atomic structure of the bulk $MnBi_2Te_4$ (Figure 1e) is consistent with the previous reports,[11,12,14] showing an SL structure (Te1−Bi−Te2−Mn−Te2−Bi−Te1), as depicted by the atomic model in Figure 1f. Quantitative EDS mapping (see the Methods) further revealed the chemical composition of the surface to mainly consist of Bi and Te, with trivial Mn. The ratio of Mn, Bi, and Te at the surface QL layer, highlighted by the red dashed rectangle in Figure 1g, is estimated to be ∼0.3:1.8:3 (Figure 1h), whereas it reaches the normal 1:2:4 ratio below the surface (Figure S3).

Above the QL structure, an amorphous layer with brighter contrast than the nearby graphite protection layer is observed. This amorphous layer separated from the QL surface with a clear VDW gap, as highlighted by red dashed lines in Figure 1c. Moreover, the crystalline structure with a DL height was occasionally observed to be embedded in such an amorphous layer, which is highlighted by the white arrows. A larger view of the surface (Figure 1g) further manifested that these tiny crystalline structures are omnipresent above the surface yet gapped by amorphous layers in between. EDS results of such an amorphous layer and an embedded crystalline quantum island (highlighted by the red dashed rectangle in Figure 1g) clearly reveal that in contrast with the QL layer, the major elements are Mn and Te, with trivial Bi. The element ratio among Mn, Bi, and Te is ∼0.7:0.2:1 (Figure 1i).

The cross-sectional results pointed to a critical finding that the surface of the as-prepared $MnBi_2Te_4$ few-layer sample underwent a surface collapse even with intentional surface protection during the mechanical exfoliation in an inert gas environment. Instead of the ideal SL model with the chemical composition Mn:Bi:Te of 1:2:4, which is the case below the surface, as verified by quantitative EDS, the realistic surface layer splits into a Bi-rich QL plus a Mn-rich DL crystalline/amorphous layer, with a complementary elemental distribution of 0.3:1.8:3 and 0.7:0.2:1, respectively. Such surface collapse and reconstruction are highly reproducible in all of the samples we measured, even in a mild transfer without heating during the drop-down process of the protection graphite layer. Mn-doped QL Bi_2Te_3 is stable, as previously reported,[13] but the DL Bi-doped MnTe is theoretically unstable (see Supporting Information Section II for more details) and has high reactivity. The existence of the island-like DL crystalline structure is presumably due to the VDW interaction from the underlying layers and the local chemical composition fluctuation during the surface reconstruction.

Detection of the Mn−Bi Exchange Antisite Defects by Atomic EELS, EDS, and Intensity Quantification Analysis. The unexpected surface collapse and reconstruction may be related to the superficial chemical stoichiometry variation or surface defects.[25] To further find out the cause of the surface collapse, we carried out atom-by-atom EELS across the reconstructed surface. Figure 2a shows the EELS of each atomic column in the surface QL structure, with the simultaneously collected HAADF image shown on the right. The identity of Bi shown by the M_4 edge at 2688 eV shows up only at the second and fourth layers, corresponding to the two brightest spots, which is consistent with the expected STEM HAADF intensity due to its large atomic number. The atomic EELS and simulated STEM HAADF image (see Figure S5) suggest that the surface QL is an alternating Te−Bi−Te−Bi−Te QL, similar to the Bi_2Te_3 structure. However, it is surprising that a clear Mn signal, labeled by the $L_{2,3}$ edge at 640 eV, also shows up exactly in the Bi columns. This suggests that antisite defects, Bi_{Mn} or Mn_{Bi}, may have been present on the surface even before the surface collapse occurred.

To further confirm the scenario of Bi_{Mn} or Mn_{Bi}, we also collected atomic EELS and EDS maps from the bulk SL structure. Figure 2b shows the EELS across the SL structure. Surprisingly, we found that a clear Bi signal appeared in the Mn layer (fourth atomic column in Figure 2b), whereas a strong Mn signal appeared in both of the Bi layers (second and sixth layers), evidencing the presence of Bi_{Mn} and Mn_{Bi}. As a result, the Mn layer has much brighter intensity than the simulated STEM HAADF image, which used the ideal SL model (Figure S5), due to the inclusion of the heavier Bi atoms and vice versa. In contrast, Te layers showed no Mn or Bi signals, excluding the presence of other types of antisite defects. Such behavior was also shown by the atomic-resolution EDS mapping in the bulk SL structure, as shown in Figure 2d, where clear Bi and Mn intermixing signals are detected in all Bi and Mn atomic columns but not in the Te layers. However, the elemental distribution of an SL in the bulk was exactly 1:2:4, as probed by EDS, which implied the occurrence of intralayer exchange between Bi and Mn atoms. Therefore, such Mn−Bi intralayer exchange results in an almost equal amount of Bi_{Mn} and Mn_{Bi} in both Mn and Bi layers.

To further investigate the Mn−Bi intralayer exchange effect quantitatively, we mapped the intensity of all atomic columns in the SL structure on a large scale using a peak intensity finding software[26] and performed the quantitative statistical analysis. Figure 2c shows the intensity histogram. Mn, Bi, and Te sites are mapped separately, as indicated by the markers shown on the representative STEM image. To quantitatively study the intralayer exchange between the Mn and Bi layers, we compared the experimental value to the simulations. The dark-gray dashed lines in Figure 2c are the simulated intensities of Mn, Bi, and Te columns using the ideal SL structure without any antisite defects, where the Te column is normalized to the experimental value for direct comparison. As expected, the intensity of all Mn columns is much higher than the simulated one, whereas the intensity of Bi is lower, and both had a wider distribution than Te, which is direct evidence of intralayer Mn−Bi intermixing. From the simulated intensity, when the concentration of Bi_{Mn} reaches 30% in the Mn layer, the intensity of the Mn atomic column is almost similar to that of Te. (See Figure S5c.) The average concentration of the antisite defects in both Mn and Bi layers can be qualitatively estimated by comparing the full width at half-maximum (fwhm) of the intensity distribution with the simulation. The Bi_{Mn} concentration in the Mn layer is found to be 40∼50%, which is approximately twice the value of Mn_{Bi} concentration in Bi atomic layers. The atomic EDS analysis also supports such a high Mn−Bi interchangeable ratio, with the Bi_{Mn} concentration

https://dx.doi.org/10.1021/acsnano.0c03149
ACS Nano 2020, 14, 11262−11272

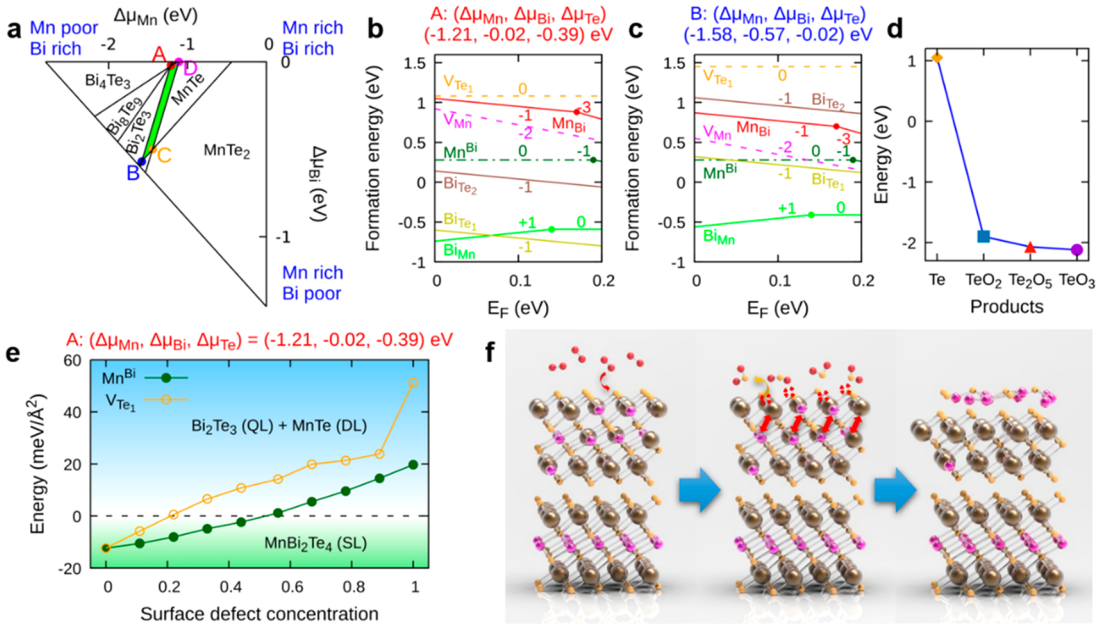

Figure 3. Physical origin of the surface collapse in $MnBi_2Te_4$. (a) Allowed chemical potential domain (green area) for $MnBi_2Te_4$ shown in the ($\Delta\mu_{Mn}$, $\Delta\mu_{Bi}$) parameter space, which is sketched out by points A, B, C, and D. The other regions are excluded due to the formation of competing phases specified in the figure. (b,c) Formation energies of defects in $MnBi_2Te_4$ for chemical potential sets A and B shown in panel a. Formation energies at C and D are shown in the Supporting Information. (d) Calculated formation energy of V_{Te1} for different tellurium oxides. (e) Relative surface energy as a function of defect concentration under chemical potential set A. The dashed line indicates the energy of the surface terminating with Bi_2Te_3 and MnTe islands. (f) Schematic of the surface collapse and reconstruction in the $MnBi_2Te_4$ crystal induced by the formation of an oxygen-driven Te vacancy and the subsequent Mn−Bi exchange effect.

in the Mn layer being 40∼50% and the Mn_{Bi} concentration in the Bi atomic layers being approximately 20∼30%. These results are consistent with our previous analysis that the amount of Bi_{Mn} and Mn_{Bi} should be equal due to the intralayer exchange, whereas the amount of Bi is double the amount of Mn due to the 1:2:4 chemical stoichiometry.

Physical Origin of the Defect-Triggered Surface Collapse and Reconstruction. To uncover the physical origin of the observed surface reconstruction in $MnBi_2Te_4$, we carried out comprehensive thermodynamic defect calculations by using the DFT. By far, our experiments evidenced that high concentrations of intrinsic antisite defects (Bi_{Mn} and Mn_{Bi}) are presented in the Mn and Bi layers, and thus we first examined the formation of antisite defects due to the Bi−Mn exchange in $MnBi_2Te_4$. The chemical potential substantially affects the calculations of defect formation energy. Therefore, we determined the accessible range of the chemical potential, that is, the growth condition, of $MnBi_2Te_4$ in the ($\Delta\mu_{Mn}$, $\Delta\mu_{Bi}$) parameter space with the constraints imposed by competing binary compounds, as shown in the green area of Figure 3a. In the unstable regions (white area), $MnBi_2Te_4$ tends to decompose to various competing phases. Therefore, the formation energies of native defects were calculated under merely two representative environments, that is, the Bi-rich condition ($\Delta\mu_{Bi} \approx 0$ eV) and the Te-rich condition ($\Delta\mu_{Te} \approx 0$ eV), denoted by the A and B points in Figure 3a, respectively. More information about the defect calculations is provided in Supporting Information Sections III−IV.

For the Bi-rich condition (see Figure 3b), Bi_{Mn}, having the lowest formation energy, is the dominant donor defect due to the excess valence electrons of Bi compared with Mn. On the contrary, the cation-to-cation antisite defect (Mn_{Bi}) has a much lower formation energy than the anion-to-cation antisite defect (Te_{Bi}), even under Te-rich conditions (Figure S7), and thus Bi_{Mn} and Mn_{Bi} are two dominant defects in $MnBi_2Te_4$. The combination of these two antisite defects creates a double defect of Mn−Bi exchange (Mn^{Bi}), with relatively small formation energies shown as the dark-green line of Figure 3b,c. This explains the high concentration of the cation-to-cation antisite exchange defects observed in the STEM cross-section image. Note that to form Mn^{Bi}, no atom exchange between $MnBi_2Te_4$ and the reservoirs is required.

The physical origin of the ideal SL to the as-observed reconstructed surface (QL+DL structure) should be closely related to the defect landscape of $MnBi_2Te_4$. First, we consider the total energy of $MnBi_2Te_4$ with Mn^{Bi} exchange defects at the surface and compare with the total energy of Bi_2Te_3 and MnTe islands under surface reconstruction. The latter is set to 0 as the reference, denoted by the dashed line in Figure 3e. We find that the energy of the defective SL surface increases monotonically with the increasing Mn^{Bi} concentration, which is consistent with its positive defect formation energy from our calculation. (See Supporting Information Section V for calculation models and methods.) To pass the reference line and thus realize the collapse from SL to QL, the required concentration of Mn^{Bi} is extremely high (>50%). Such a high defect concentration is not observed in our experiments because the bulk still has a stable SL framework against reconstruction; only the surface did undergo such reconstruction. In other words, although Mn^{Bi} is the dominant defect under the equilibrium growth conditions, Mn^{Bi} alone can hardly promote the SL surface collapse into the QL. Therefore, the driving force of the surface collapse should be something else, most likely some defects that may form at the surface regardless of their relatively large formation energies in the bulk.

https://dx.doi.org/10.1021/acsnano.0c03149
ACS Nano 2020, 14, 11262−11272

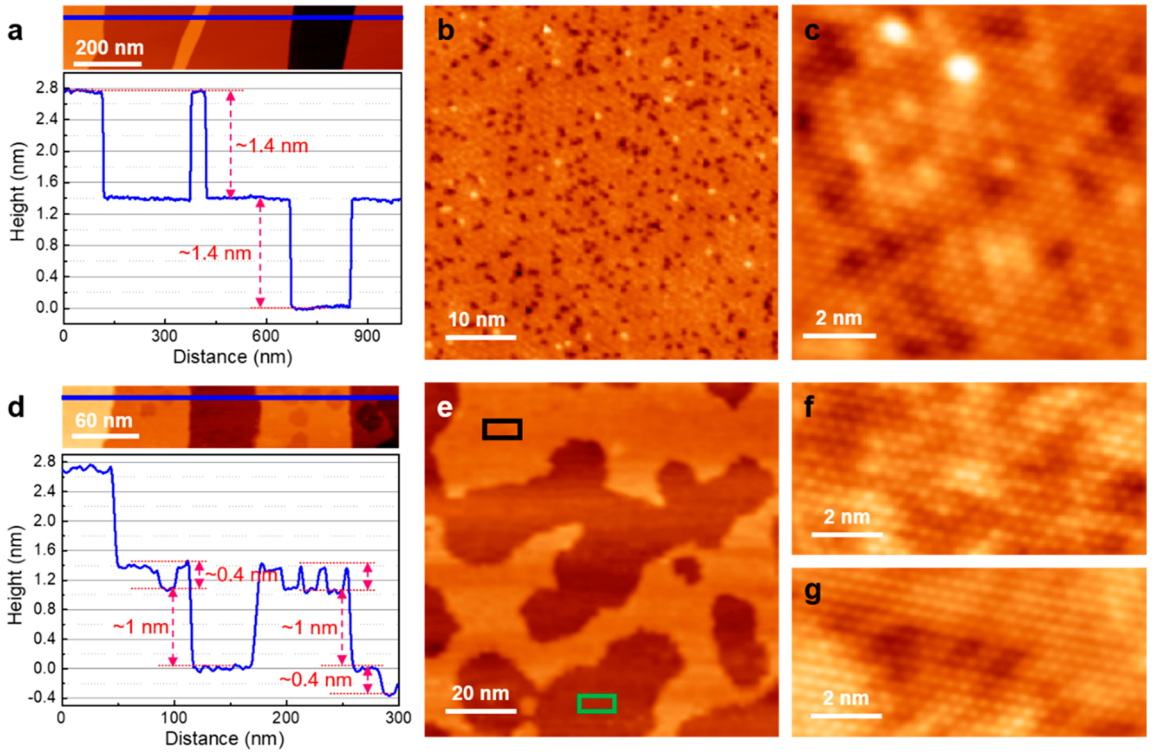

Figure 4. ***In situ*** **heating of the exfoliated $MnBi_2Te_4$ surface in an ultrahigh vacuum. (a) Large-scale STM image of $MnBi_2Te_4$ (00*l*) surface exfoliated in an ultrahigh vacuum and the corresponding height line profile along the blue line. (b) Zoom-in STM image of the $MnBi_2Te_4$ (00*l*) surface with defects. (c) Atomic-resolution image of the $MnBi_2Te_4$ surface. The dark spots are concluded to be the Bi^{Mn} antisite defects under the Te layer. The SL height and the crystalline surface imply that the intact $MnBi_2Te_4$ surface can be preserved in an ultrahigh vacuum. (d) Large-scale STM image of the *in situ* heated $MnBi_2Te_4$ surface and the corresponding height line profile along the blue line. Holes with DL heights appear after heating. (e) Zoom-in image of the annealed surface. (f,g) Atomically resolved STM images of the annealed surface marked by black and green boxes in panel e, respectively. Tunneling parameters: (a) V_{bias}= 1 V, I_t= 200 pA; (b) V_{bias}= 1 V, I_t = 50 pA; (c) V_{bias}= −1 V, I_t= 3 nA; (d) V_{bias}= 1.2 V, I_t= 20 pA; (e) V_{bias}= 1.5 V, I_t= 1 nA; (f) V_{bias}= −1 V, I_t= 1 nA; (g) V_{bias}= 0.2 V, I_t= 500 pA.**

From bulk to surface, the outermost layer (Te1 layer in $MnBi_2Te_4$) suffers the strongest environmental perturbation, such as unintentionally introduced atomic vacancies upon cleavage. It is known that tellurides like $MnBi_2Te_4$ are readily oxidized, which would break the equilibrium growth condition. Taking tellurium oxides into account, we reevaluated the formation energy of Te1 vacancy V_{Te1}. (See Supporting Information Section VI for calculation details.) As illustrated in Figure 3d, under equilibrium Te-poor conditions, the formation energy of V_{Te1} is ∼1.1 eV, indicating the relatively low V_{Te1} concentration in bulk. However, with the assistance of oxygen, instead of forming an elemental Te solid, Te forms tellurium oxides, with the V_{Te1} formation energy dramatically decreased. We consider three tellurium oxides, TeO_2, Te_2O_5, and TeO_3. For all cases, the calculated V_{Te1} formation energies are about −2 eV, indicating an exothermal reaction. The total energy of $MnBi_2Te_4$ with V_{Te1} defects at the surface quickly increases with the increase in V_{Te1} concentration, as shown in Figure 3e. To realize the SL to QL collapse, the required surface V_{Te1} concentration is ∼20% under the Bi-rich condition. With the assistance of Mn^{Bi}, the surface collapse may take place at an even lower V_{Te1} concentration. Overall, as illustrated by the schematic in Figure 3f, oxygen at the surface reacts with the Te1 sublayer, leaving tellurium vacancies. Such surface V_{Te1} serves as the dominant driving force to trigger the surface collapse and QL+DL reconstruction in the original SL $MnBi_2Te_4$ structure by accelerating the Bi−Mn exchange, which leads to the depletion of Mn in the QL, consistent with the EDS results in Figure 1h. The exchange barrier between the Bi and Mn atoms in the lattice is quite small (0.28 eV, Figure 3b), and the depletion of Mn is essential to form a QL (Bi_2Te_3) + DL (MnTe) reconstructed structure, which is energetically more favorable than the defective SL $MnBi_2Te_4$ structure with a Te vacancy, as shown in Figure 3e. Indeed, we observed a small amount of oxygen signal at the interface between the QL structure and the graphite, as detected by both EELS and EDS (see Figure S4 and Figure 1i) and also in the XPS measurement, which confirmed the contribution of oxygen to creating surface Te vacancies and the subsequent oxidation of the reconstructed outermost DL structure during the depletion of the Mn in the surface collapse process. Moreover, the theory also suggests that such surface reconstruction involves a kinetic thermal nonequilibrium. Such a process would result in an incomplete Bi−Mn exchange, which is also consistent with the chemical stoichiometry of the QL and the amorphous/crystalline DL structure, as probed by EDS. (See Figure 1h,i.)

Verifying the Defect-Induced Surface Collapse and Reconstruction by *in Situ* STM and STEM. To verify the scenario of the Te-vacancy-driven surface collapse suggested by theory, we first tried to exclude the presence of oxygen by investigating the *in situ* cleaved $MnBi_2Te_4$ surface using UHV STM. The operation pressure is better than 2×10^{-10} Torr, where the oxygen concentration is multiple orders of magnitude lower than the inert gas environment in a glovebox. Figure 4a shows the STM image of a freshly exfoliated

https://dx.doi.org/10.1021/acsnano.0c03149
ACS Nano 2020, 14, 11262−11272

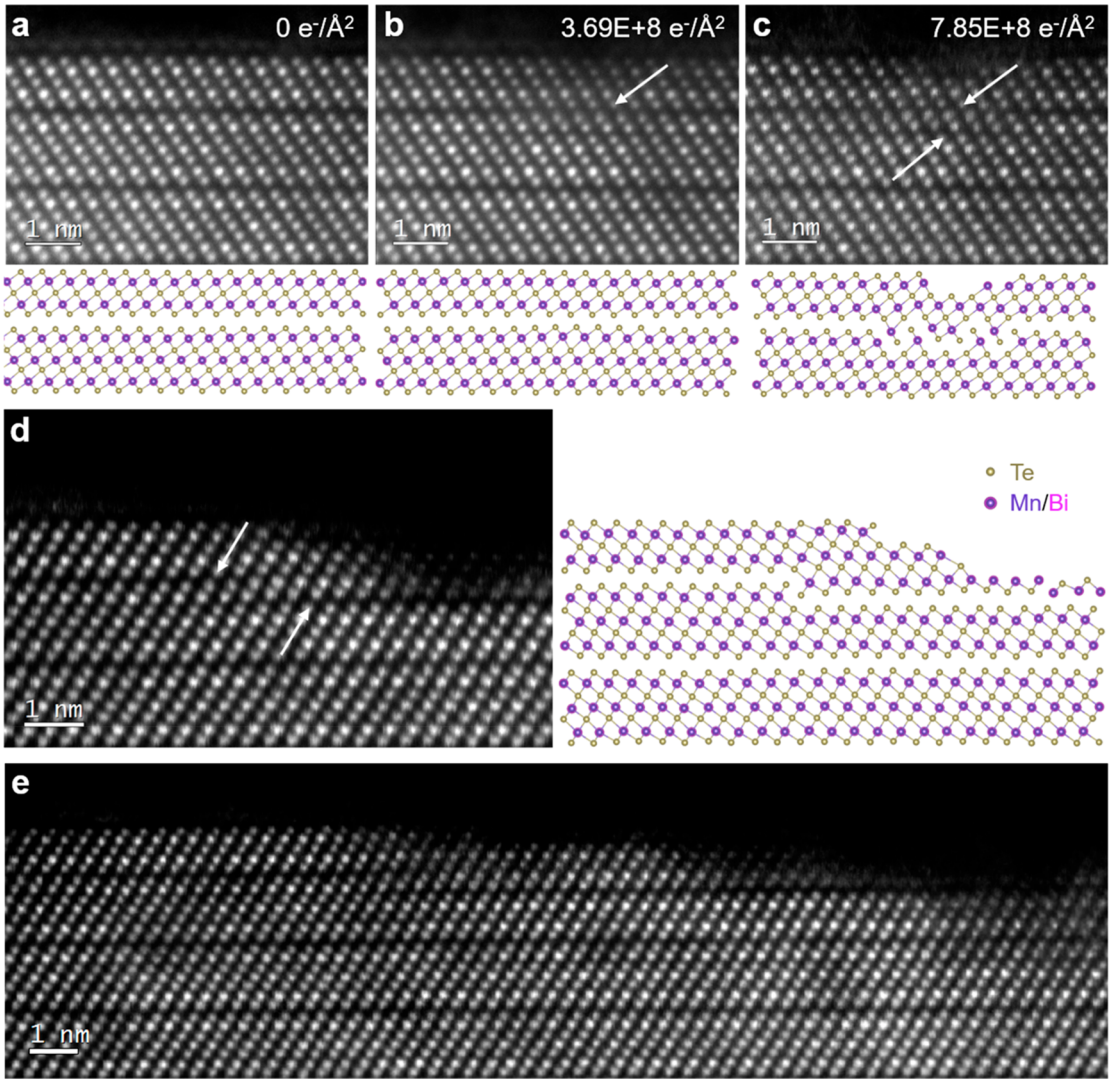

Figure 5. ***In situ*** **observation of the dynamical surface collapse and reconstruction process induced by electron irradiation. (a–c) Evolution of the surface atomic structure as a function of electron dose: (a) 0, (b) 3.69 × 10^8, and (c) 7.85 × 10^8 $e^-/Å^2$. The corresponding atomic models are shown below where the Bi and Mn atoms are not discriminated due to the massive existence of Mn^{Bi} exchange defects. The arrows in panel c indicate the close of the original VDW gap due to the loss of Te atoms, with another VDW gap opening two layers down the collapsed and reconstructed region. (d) Atomic STEM image showing a discontinue VDW gap along the surface after collapse and reconstruction. (e) STEM image showing a large scale of the surface structure after prolonged electron irradiation, where all surfaces were terminated by the QL or QL+DL structures. Note that the collapse and reconstruction process occurred under an ultrahigh vacuum.**

$MnBi_2Te_4$ single crystal terminating with the (00*l*) surface. Abrupt steps with a uniform height of ∼1.4 nm (seven atomic layers, Figure 4a) were obtained. An enlarged STM image shows an atomic crystalline surface (Figure 4b,c) with randomly distributed dark spots. According to the bias-voltage-dependent STM images of these dark spots (see Figure S9), they are ascribed to the Bi^{Mn} antisite defects underneath the Te layer, which is consistent with our STEM results and the previous report.[27] This indeed confirmed that the ideal SL $MnBi_2Te_4$ surface can be preserved in a UHV.

To introduce Te vacancies at the surface, an *in situ* heating at 150 °C was then applied to the surface for ∼41 h because Te is easily sublimated at an elevated temperature. An apparent structure collapse is observed, evidenced by the emergence of holes with a step height of ∼0.4 nm (two atomic layers, Figure 4d) inside the originally flat surface. (See Figure 4e.) As a result, the height of the collapsed region, as shown by the dimmer contrast in Figure 4e, is ∼1 nm (the height profile in Figure 4d), corresponding to five atomic layers. The collapsed surface still shows a similar atomic crystalline structure with hexagonal patterns (Figure 4h,g) due to the surface similarity between $MnBi_2Te_4$ and Bi_2Te_3.

The STM results point out that the elevated temperature can induce a similar surface collapse by sublimating surface Te atoms. Therefore, to rule out the heating effect from the high-energy Ga ions during the cross-sectional sample preparation in the focused ion beam (FIB), we carried out cryo-FIB to prepare the TEM sample in a high vacuum (<10^{-6} mbar) and at liquid-nitrogen temperature (−140 °C). The surface of $MnBi_2Te_4$ still displays the same QL plus the DL amorphous/crystalline structure (Figure S10), which further certified that the surface reconstruction indeed occurred during the mechanical exfoliation in the inert gas environment.

The above results are in agreement with the surface collapse and reconstruction mechanism suggested by theory. We also attempted to capture the dynamical process of the collapsed

https://dx.doi.org/10.1021/acsnano.0c03149
ACS Nano 2020, 14, 11262–11272

surface reconstruction directly. It is well known that the use of high-energy electrons in imaging also simultaneously transfers momentum and energy to the specimen, which can result in beam-induced defects.[28] Figure 5a–c shows sequential STEM images as a function of the electron dose, highlighting the dynamical surface collapse and reconstruction process on the $MnBi_2Te_4$ surface. As the electron dose accumulates, the atomic column intensity of the outermost layer (Te1 layer in the QL structure) is dimmed due to the loss of tellurium (Figure 5b). Meanwhile, the gap between the surface QL and the next SL, which is underneath the Te loss region, as highlighted by the arrow in Figure 5b, narrows from 2.6 to2 Å. A significant split is seen in the first two atomic layers of the SL, a trend in the separation into a DL and a QL structure. Finally, as the two outermost atomic columns are eliminated by electron bombardment, the surface structure collapses and reconstructs from a QL+SL to double QLs (Figure 5c).

The dynamical collapse and reconstruction process indicates that the VDW gap can close and reopen during the formation of defects depending on the exact layer configurations. This indeed means that the VDW gap between layers can be discontinued in a reconstructed surface as long as the outermost surface is a QL structure, which is highlighted by the white arrows in Figure 5d. Moreover, once the surface QL got damaged by the electron irradiation, the SL structure underneath would also quickly reconstruct to form a stable QL, indicating the extreme instability of the SL structure under perturbation, which may not survive as the outermost surface. This is evidenced in Figure 5e, which shows a large view of the collapsed and reconstructed surface, including QL+SL, two QL, and DL+QL structures, all of which manifest the QL as the stable surface structure. The *in situ* dynamical imaging unambiguously confirmed that the formation of a Te vacancy leads to the surface collapse and reconstruction in the $MnBi_2Te_4$ single crystal.

Our results reveal that the surface structure of $MnBi_2Te_4$ is not as stable as previously thought, a condition that inevitably effects the surface electronic structure and thus the topological surface-bulk correspondence. Theoretically, when the surface inherits the crystal and magnetic structures of the bulk, a gapped Dirac cone with dozens of millielectronvolts is expected due to the intrinsic magnetism. However, high-resolution ARPES measurements unambiguously show a robust gapless Dirac cone at the $MnBi_2Te_4$ surface.[16,23,24] One possibility is that the local moments of Mn atoms tend to distribute randomly, giving rise to the almost zero band gap with linear dispersion. However, direct experimental evidence, such as surface magnetic configurations, is still lacking to support this hypothesis. Here we suggest from our experimental results that the surface collapse leads to a significant absence of the magnetic atoms together with magnetic disorder, resulting in a vanishing surface gap. First of all, with the surface $MnBi_2Te_4$ SL collapsing to the Bi_2Te_3 QL, the origin of the Dirac gap opening is mainly the proximity effect from the ordered magnetic moments of the second topmost SL. Compared with the perfect SL surface, the proximity-induced gap is much smaller. To confirm this, we calculated by DFT the surface electronic structure with both terminations, that is, the perfect $MnBi_2Te_4$ SL and the collapsed Bi_2Te_3 QL. As shown in Figure S11, compared with the $MnBi_2Te_4$ termination without surface collapse and reconstruction, the surface band gap of $MnBi_2Te_4$ with the surface layers degraded to Bi_2Te_3 shows a significant reduction (from 42 to 5 meV). In addition, residual MnTe DL islands on the Bi_2Te_3 QL surface tend to be antiferromagnetic with parallel Mn spins in the basal plane.[29,30] Therefore, the floating Mn atoms in the DL atoms cannot help to open the surface Dirac gap either. Finally, our findings suggest that the device application of thin-film $MnBi_2Te_4$, for example, the quantum anomalous Hall effect, may also suffer from the impact of the surface collapse and reconstruction, which calls for further exploration.

CONCLUSIONS

In summary, we have discovered that a vacancy-induced surface collapse and reconstruction in an exfoliated $MnBi_2Te_4$ single crystal occurs even under the protection of a well-controlled inert gas environment. Combining STEM imaging, STM experiments, and DFT calculations, we systematically show that such surface collapse results from the synergistic effect of the high-concentration intrinsic Mn–Bi exchange defects and the formation of a tellurium vacancy on the surface, which is induced by the trace of oxygen in the inert gas environment. The surface reconstruction and the existence of massive intrinsic defects bring a more comprehensive understanding of the antiferromagnetism and the anomalous quantum states of $MnBi_2Te_4$ few-layer devices. The discovery of such a sensitive surface not only provides an insightful perspective on all $MnBi_2Te_4$ few-layer devices fabricated in a non-UHV environment but also sheds light on understanding the surface-related measurements, the exploration of exotic quantum phenomena, and the device fabrication for applications based on the $MnBi_2Te_4$ crystal.

MATERIALS AND METHODS

Sample Fabrication. The few-layer $MnBi_2Te_4$ was exfoliated from bulk $MnBi_2Te_4$ through a Scotch-tape method in a glovebox filled with argon. The parent $MnBi_2Te_4$ bulk crystal was grown by the flux method.[16] The fresh surface was exposed to an argon atmosphere and subsequently covered by graphite through a routine dry-transfer method in the glovebox to encapsulate the surface from being oxidized. To eliminate the possible impact of graphite, we prepared multiple samples of $MnBi_2Te_4$ covered by graphite with different thicknesses. The graphite layer was exfoliated and transferred to $MnBi_2Te_4$ immediately after a fresh cleavage. The same surface reconstruction was observed in all samples, proving that the graphite layer merely served as the surface protection against further oxidization. The cross-section STEM specimens were quickly prepared using a FIB and a cryo-FIB in a UHV ($<10^{-6}$ mbar) and under a liquid-nitrogen temperature (−140 °C) environment after the sample was fetched from the glovebox, all of which ensured minimum surface degradation.

Characterizations. *X-ray Diffraction.* Single-crystal XRD was performed on a Rigaku MiniFlex diffractometer using Cu Kα radiation at room temperature.

X-ray Photoelectron Spectroscopy. The XPS measurement on the freshly exfoliated surface of the $MnBi_2Te_4$ crystal was performed on a PHI 5000 Versaprobe III apparatus. The spectrum was analyzed by the PHI-MultiPak software.

Atomic Force Microscopy. The AFM measurement was carried out using the Asylum Research Cypher S system placed in an inert gas environment. To minimize the oxidation of $MnBi_2Te_4$, the exfoliation of the $MnBi_2Te_4$ crystal and AFM measurements were performed one after another in the same glovebox.

Scanning Tunneling Microscopy. The STM experiments were carried out with a low-temperature STM (UNISOKU, USM1500) under UHV conditions. The $MnBi_2Te_4$ single crystal was cleaved along the (00*l*) crystal plane in the STM chamber with a base pressure of 2×10^{-10} mbar. The freshly cleaved sample was immediately

https://dx.doi.org/10.1021/acsnano.0c03149
ACS Nano 2020, 14, 11262–11272

transferred to the STM chamber for further measurements at 78 K (or 5 K). The sample was baked at 150 °C for 41 h to introduce surface reconstruction. The tungsten tip was prepared by electrochemical etching and subsequent e-beam heating and Ar^+ sputtering. We trained the tip apex on a clean Cu (111) surface prior to all measurements. STM topography images were processed by WSxM.[31]

Scanning Transmission Electron Microscopy. STEM imaging and EDS and EELS analysis of the $MnBi_2Te_4$ crystal were performed on an FEI Titan Themis apparatus with an X-FEG electron gun and a DCOR aberration corrector operating at 300 kV. The inner and outer collection angles for the STEM images (β_1 and β_2) were 48 and 200 mrad, respectively. The convergence semiangle of the probe was 25 mrad. The beam current was ~100 pA for high-angle annular dark-field imaging and the EDS and EELS chemical analyses. All imaging was performed at room temperature. The ratios between Mn, Bi, and Te were normalized based on the bulk $MnBi_2Te_4$ crystal. Thereinto, in the electronic irradiation experiment, the electron dose (D) was calculated by $D = I \times T/A$ using the beam current (I), beam illuminating area (A), and the irradiation time (T).

Density Functional Theory Calculations. First-principles calculations were carried out using the Vienna *ab initio* simulation package (VASP)[32] within the framework of the DFT.[33] The exchange-correlation functional was described by the generalized gradient approximation with the Perdew–Burke–Ernzerhof (PBE) formalism.[34] The electron–ion interaction was treated by projector-augmented-wave (PAW) potentials[35] with a planewave-basis cuff of 500 eV. The whole Brillouin zone was sampled by the Monkhorst–Pack grid[36] for all models. Because of the correlation effects of 3d electrons in Mn atoms, we employed the GGA+U approach within the Dudarev scheme and set the U to be 5 eV, which was investigated by a previous work.[16] All atoms were fully relaxed until the force on each atom was <0.01 eV/Å and the total energy minimization was performed with a tolerance of 10^{-5} eV. Freely available software VASPKIT[37] was used to deal with VASP output files. The calculation process is detailed in Supporting Information Sections II–VI.

ASSOCIATED CONTENT

Supporting Information

The Supporting Information is available free of charge at https://pubs.acs.org/doi/10.1021/acsnano.0c03149.

Further experimental and theoretical details, including XPS chemical analysis and AFM characterizations of the $MnBi_2Te_4$ single crystal at the cleaved surface, more cross-sectional STEM images of the $MnBi_2Te_4$ surface and the corresponding EDS and EELS mapping, the statistical intensity variation in STEM images with different concentrations of exchange Mn–Bi defects, phonon dispersion of the MnTe DL structure, the formation energies of various defects in $MnBi_2Te_4$ under different chemical environments, relative surface energy with different defect concentrations, and DFT-calculated surface band structures of $MnBi_2Te_4$ SL and Bi_2Te_3 QL terminations (PDF)

AUTHOR INFORMATION

Corresponding Authors

Junhao Lin − *Department of Physics and Shenzhen Key Laboratory of for Advanced Quantum Functional Materials and Devices, Southern University of Science and Technology, Shenzhen 518055, Guangdong, P. R. China;* orcid.org/0000-0002-2195-2823; Email: linjh@sustech.edu.cn

Qihang Liu − *Department of Physics, Shenzhen Institute for Quantum Science and Engineering, Guangdong Provincial Key Laboratory for Computational Science and Material Design, and Shenzhen Key Laboratory of for Advanced Quantum Functional Materials and Devices, Southern University of Science and Technology, Shenzhen 518055, Guangdong, P. R. China;* Email: liuqh@sustech.edu.cn

Yue Zhao − *Department of Physics and Shenzhen Institute for Quantum Science and Engineering, Southern University of Science and Technology, Shenzhen 518055, Guangdong, P. R. China;* orcid.org/0000-0002-9174-0519; Email: zhaoy@sustech.edu.cn

Authors

Fuchen Hou − *Department of Physics and Shenzhen Key Laboratory of for Advanced Quantum Functional Materials and Devices, Southern University of Science and Technology, Shenzhen 518055, Guangdong, P. R. China*

Qiushi Yao − *Department of Physics, Southern University of Science and Technology, Shenzhen 518055, Guangdong, P. R. China*

Chun-Sheng Zhou − *Department of Physics, Southern University of Science and Technology, Shenzhen 518055, Guangdong, P. R. China*

Xiao-Ming Ma − *Department of Physics, Southern University of Science and Technology, Shenzhen 518055, Guangdong, P. R. China*

Mengjiao Han − *Department of Physics and Shenzhen Key Laboratory of for Advanced Quantum Functional Materials and Devices, Southern University of Science and Technology, Shenzhen 518055, Guangdong, P. R. China*

Yu-Jie Hao − *Department of Physics, Southern University of Science and Technology, Shenzhen 518055, Guangdong, P. R. China*

Xuefeng Wu − *Department of Physics, Southern University of Science and Technology, Shenzhen 518055, Guangdong, P. R. China*

Yu Zhang − *Department of Physics, Southern University of Science and Technology, Shenzhen 518055, Guangdong, P. R. China; Department of Physics, University of Hong Kong, Hong Kong, P. R. China*

Hongyi Sun − *Department of Physics, Southern University of Science and Technology, Shenzhen 518055, Guangdong, P. R. China*

Chang Liu − *Department of Physics and Shenzhen Institute for Quantum Science and Engineering, Southern University of Science and Technology, Shenzhen 518055, Guangdong, P. R. China*

Complete contact information is available at: https://pubs.acs.org/10.1021/acsnano.0c03149

Author Contributions

#F.H. and Q.Y. contributed equally to this work. J.L. conceived the project. F.H. and J.L. made the TEM samples and performed AFM measurements and STEM-related experiments, analysis, and simulations. DFT calculations were done by Q.Y., H.S., and Q.L. Sample growth and X-ray analysis was done by X.-M.M., Y.-J.H., and C.L. STM measurements were carried out by C.-S.Z., X.W., Y. Zhang, and Y. Zhao. J.L. constructed the schematic of the $MnBi_2Te_4$ surface collapse and reconstruction. M.H. participated in parts of the STEM experiments. The work was coordinated by J.L., Q.L. and Y.Z. The manuscript was written by J.L., F.H., Q.L., and Q.Y. with input from all authors. All authors commented on the manuscript.

Notes

The authors declare no competing financial interest.

https://dx.doi.org/10.1021/acsnano.0c03149
ACS Nano 2020, 14, 11262–11272

This work was previously submitted to a preprint server: Hou, F. C.; Yao, Q. S.; Zhou, C. S.; Ma, X. M.; Han, M. J.; Hao, Y. J.; Wu, X. F.; Zhang, Y.; Sun, H.Y.; Liu, C.; Zhao, Y.; Liu, Q. H.; Lin, J. H. Spontaneous Surface Collapse and Reconstructionin Antiferromagnetic Topological Insulator $MnBi_2Te_4$. 2020, arXiv:2004.08138. arXiv.orge-Print archive. https://arxiv.org/abs/2004.08138 (accessed April 17, 2020)..

ACKNOWLEDGMENTS

We thank J. Zhang for the support of XPS measurements. We acknowledge the support from the National Natural Science Foundation of China (grant no. 11974156, 11874195, 11674149 and 11674150), the Guangdong International Science Collaboration Project (grant no. 2019A050510001 and 2017ZT07C062), the National Key Research and Development Program (grant no. 2019YFA0704901), the Guangdong Provincial Key Laboratory of Computational Science and Material Design (grant no. 2019B030301001), the Key-Area Research and Development Program of Guangdong Province (2019B010931001), the Guangdong Innovative and Entrepreneurial Research Team Program (grant no. 2016ZT06D348, 2017ZT07C062, and 2019ZT08C044), the Highlight Project (No.PHYS-HL-2020-1) of the College of Science, SUSTech., and the Science, Technology and Innovation Commission of Shenzhen Municipality (nos. ZDSYS20190902092905285 and KQTD20190929173815000) and also the assistance of the SUSTech Core Research Facilities, in particular, the technical support from the Cryo-EM Center and the Pico-Centre, which receives support from the Presidential Fund and Development and Reform Commission of Shenzhen Municipality. First-principles calculations were also supported by the Center for Computational Science and Engineering at SUSTech.

REFERENCES

(1) Hasan, M. Z.; Kane, C. L. Colloquium: Topological Insulators. *Rev. Mod. Phys.* **2010**, *82*, 3045−3067.
(2) Qi, X.-L.; Zhang, S.-C. Topological Insulators and Superconductors. *Rev. Mod. Phys.* **2011**, *83*, 1057−1110.
(3) Yu, R.; Zhang, W.; Zhang, H. J.; Zhang, S. C.; Dai, X.; Fang, Z. Quantized Anomalous Hall Effect in Magnetic Topological Insulators. *Science* **2010**, *329*, 61−64.
(4) Chang, C. Z.; Zhang, J.; Feng, X.; Shen, J.; Zhang, Z.; Guo, M.; Li, K.; Ou, Y.; Wei, P.; Wang, L. L.; Ji, Z. Q.; Feng, Y.; Ji, S.; Chen, X.; Jia, J.; Dai, X.; Fang, Z.; Zhang, S. C.; He, K.; Wang, Y.; et al. Experimental Observation of the Quantum Anomalous Hall Effect in a Magnetic Topological Insulator. *Science* **2013**, *340*, 167−170.
(5) Chang, C. Z.; Zhao, W.; Kim, D. Y.; Zhang, H.; Assaf, B. A.; Heiman, D.; Zhang, S. C.; Liu, C.; Chan, M. H. W.; Moodera, J. S. High-Precision Realization of Robust Quantum Anomalous Hall State in a Hard Ferromagnetic Topological Insulator. *Nat. Mater.* **2015**, *14*, 473−477.
(6) Soluyanov, A. A.; Gresch, D.; Wang, Z.; Wu, Q.; Troyer, M.; Dai, X.; Bernevig, B. A. Type-II Weyl Semimetals. *Nature* **2015**, *527*, 495−498.
(7) Tang, P.; Zhou, Q.; Xu, G.; Zhang, S.-C. Dirac Fermions in an Antiferromagnetic Semimetal. *Nat. Phys.* **2016**, *12*, 1100−1104.
(8) Mogi, M.; Kawamura, M.; Yoshimi, R.; Tsukazaki, A.; Kozuka, Y.; Shirakawa, N.; Takahashi, K. S.; Kawasaki, M.; Tokura, Y. A Magnetic Heterostructure of Topological Insulators as a Candidate for an Axion Insulator. *Nat. Mater.* **2017**, *16*, 516−521.
(9) He, Q. L.; Pan, L.; Stern, A. L.; Burks, E. C.; Che, X.; Yin, G.; Wang, J.; Lian, B.; Zhou, Q.; Choi, E. S.; Murata, K.; Kou, X.; Chen, Z.; Nie, T.; Shao, Q.; Fan, Y.; Zhang, S.-C.; Liu, K.; Xia, J.; Wang, K. L. Chiral Majorana Fermion Modes in a Quantum Anomalous Hall Insulator-Superconductor Structure. *Science* **2017**, *357*, 294−299.
(10) Tokura, Y.; Yasuda, K.; Tsukazaki, A. Magnetic Topological Insulators. *Nat. Rev. Phys.* **2019**, *1*, 126−143.
(11) Li, J.; Li, Y.; Du, S.; Wang, Z.; Gu, B.-L.; Zhang, S.-C.; He, K.; Duan, W.; Xu, Y. Intrinsic Magnetic Topological Insulators in van der Waals Layered $MnBi_2Te_4$-Family Materials. *Sci. Adv.* **2019**, *5*, No. eaaw5685.
(12) Li, H.; Liu, S.; Liu, C.; Zhang, J.; Xu, Y.; Yu, R.; Wu, Y.; Zhang, Y.; Fan, S. Antiferromagnetic Topological Insulator $MnBi_2Te_4$: Synthesis and Magnetic Properties. *Phys. Chem. Chem. Phys.* **2020**, *22*, 556.
(13) Rienks, E. D. L.; Wimmer, S.; Sánchez-Barriga, J.; Caha, O.; Mandal, P. S.; Ružička, J.; Ney, A.; Steiner, H.; Volobuev, V. V.; Groiss, H.; Albu, M.; Kothleitner, G.; Michalička, J.; Khan, S. A.; Minár, J.; Ebert, H.; Bauer, G.; Freyse, F.; Varykhalov, A.; Rader, O.; et al. Large Magnetic Gap at the Dirac Point in $Bi_2Te_3/MnBi_2Te_4$ Heterostructures. *Nature* **2019**, *576*, 423−428.
(14) Gong, Y.; Guo, J.; Li, J.; Zhu, K.; Liao, M.; Liu, X.; Zhang, Q.; Gu, L.; Tang, L.; Feng, X.; Zhang, D.; Li, W.; Song, C.; Wang, L.; Yu, P.; Chen, X.; Wang, Y.; Yao, H.; Duan, W.; Xu, Y.; et al. Experimental Realization of an Intrinsic Magnetic Topological Insulator. *Chin. Phys. Lett.* **2019**, *36*, 076801.
(15) Liu, C.; Wang, Y.; Li, H.; Wu, Y.; Li, Y.; Li, J.; He, K.; Xu, Y.; Zhang, J.; Wang, Y. Robust Axion Insulator and Chern Insulator Phases in a Two-Dimensional Antiferromagnetic Topological Insulator. *Nat. Mater.* **2020**, *19*, 522−527.
(16) Hao, Y.-J.; Liu, P.; Feng, Y.; Ma, X.-M.; Schwier, E. F.; Arita, M.; Kumar, S.; Hu, C.; Lu, R.; Zeng, M.; Wang, Y.; Hao, Z.; Sun, H.; Zhang, K.; Mei, J.; Ni, N.; Wu, L.; Shimada, K.; Chen, C.; Liu, Q.; et al. Gapless Surface Dirac Cone in Antiferromagnetic Topological Insulator $MnBi_2Te_4$. *Phys. Rev. X* **2019**, *9*, 041038.
(17) Ge, J.; Liu, Y.; Li, J.; Li, H.; Luo, T.; Wu, Y.; Xu, Y.; Wang, J. High-Chern-Number and High-Temperature Quantum Hall Effect without Landau Levels. *Natl. Sci. Rev.* **2020**, *7*, No. 1280.
(18) Otrokov, M. M.; Rusinov, I. P.; Blanco-Rey, M.; Hoffmann, M.; Vyazovskaya, A. Y.; Eremeev, S. V.; Ernst, A.; Echenique, P. M.; Arnau, A.; Chulkov, E. V. Unique Thickness-Dependent Properties of the van der Waals Interlayer Antiferromagnet $MnBi_2Te_4$ Films. *Phys. Rev. Lett.* **2019**, *122*, 107202.
(19) Otrokov, M. M.; Klimovskikh, I. I.; Bentmann, H.; Estyunin, D.; Zeugner, A.; Aliev, Z. S.; Gaß, S.; Wolter, A. U. B.; Koroleva, A. V.; Shikin, A. M.; Blanco-Rey, M.; Hoffmann, M.; Rusinov, I. P.; Vyazovskaya, A. Y.; Eremeev, S. V.; Koroteev, Y. M.; Kuznetsov, V. M.; Freyse, F.; Sánchez-Barriga, J.; Amiraslanov, I. R.; et al. Prediction and Observation of an Antiferromagnetic Topological Insulator. *Nature* **2019**, *576*, 416−422.
(20) Mong, R. S. K.; Essin, A. M.; Moore, J. E. Antiferromagnetic Topological Insulators. *Phys. Rev. B: Condens. Matter Mater. Phys.* **2010**, *81*, 245209.
(21) Zhang, D.; Shi, M.; Zhu, T.; Xing, D.; Zhang, H.; Wang, J. Topological Axion States in the Magnetic Insulator $MnBi_2Te_4$ with the Quantized Magnetoelectric Effect. *Phys. Rev. Lett.* **2019**, *122*, 206401.
(22) Deng, Y.; Yu, Y.; Shi, M. Z.; Guo, Z.; Xu, Z.; Wang, J.; Chen, X. H.; Zhang, Y. Quantum Anomalous Hall Effect in Intrinsic Magnetic Topological Insulator $MnBi_2Te_4$. *Science* **2020**, *367*, 895−900.
(23) Chen, Y. J.; Xu, L. X.; Li, J. H.; Li, Y. W.; Wang, H. Y.; Zhang, C. F.; Li, H.; Wu, Y.; Liang, A. J.; Chen, C.; Jung, S. W.; Cacho, C.; Mao, Y. H.; Liu, S.; Wang, M. X.; Guo, Y. F.; Xu, Y.; Liu, Z. K.; Yang, L. X.; Chen, Y. L. Topological Electronic Structure and Its Temperature Evolution in Antiferromagnetic Topological Insulator $MnBi_2Te_4$. *Phys. Rev. X* **2019**, *9*, 041040.
(24) Li, H.; Gao, S.-Y.; Duan, S.-F.; Xu, Y.-F.; Zhu, K.-J.; Tian, S.-J.; Gao, J.-C.; Fan, W.-H.; Rao, Z.-C.; Huang, J.-R.; Li, J.-J.; Yan, D.-Y.; Liu, Z.-T.; Liu, W.-L.; Huang, Y.-B.; Li, Y.-L.; Liu, Y.; Zhang, G.-B.; Zhang, P.; Kondo, T.; Shin, S.; Lei, H.-C.; Shi, Y.-G.; Zhang, W.-T.; Weng, H.-M.; Qian, T.; Ding, H. Dirac Surface States in Intrinsic

https://dx.doi.org/10.1021/acsnano.0c03149
ACS Nano 2020, 14, 11262−11272

Magnetic Topological Insulators $EuSn_2As_2$ and $MnBi_{2n}Te_{3n+1}$. *Phys. Rev. X* **2019**, *9*, 041039.
(25) Lin, J.; Zuluaga, S.; Yu, P.; Liu, Z.; Pantelides, S. T.; Suenaga, K. Novel Pd_2Se_3 Two-Dimensional Phase Driven by Interlayer Fusion in Layered $PdSe_2$. *Phys. Rev. Lett.* **2017**, *119*, 016101.
(26) Zhang, Q.; Zhang, L. Y.; Jin, C. H.; Wang, Y. M.; Lin, F. CalAtom: A Software for Quantitatively Analysing Atomic Columns in a Transmission Electron Microscope Image. *Ultramicroscopy* **2019**, *202*, 114−120.
(27) Yan, J.-Q.; Zhang, Q.; Heitmann, T.; Huang, Z.; Chen, K. Y.; Cheng, J.-G.; Wu, W.; Vaknin, D.; Sales, B. C.; McQueeney, R. J. Crystal Growth and Magnetic Structure of $MnBi_2Te_4$. *Phys. Rev. Mater.* **2019**, *3*, 064202.
(28) Hong, J.; Pan, Y.; Hu, Z.; Lv, D.; Jin, C.; Ji, W.; Yuan, J.; Zhang, Z. Direct Imaging of Kinetic Pathways of Atomic Diffusion in Monolayer Molybdenum Disulfide. *Nano Lett.* **2017**, *17*, 3383−3390.
(29) Kriegner, D.; Výborný, K.; Olejník, K.; Reichlová, H.; Novák, V.; Marti, X.; Gazquez, J.; Saidl, V.; Němec, P.; Volobuev, V. V.; Springholz, G.; Holý, V.; Jungwirth, T. Multiple-Stable Anisotropic Magnetoresistance Memory in Antiferromagnetic MnTe. *Nat. Commun.* **2016**, *7*, 11623.
(30) He, Q. L.; Yin, G.; Grutter, A. J.; Pan, L.; Che, X.; Yu, G.; Gilbert, D. A.; Disseler, S. M.; Liu, Y.; Shafer, P.; Zhang, B.; Wu, Y.; Kirby, B. J.; Arenholz, E.; Lake, R. K.; Han, X.; Wang, K. L. Exchange-Biasing Topological Charges by Antiferromagnetism. *Nat. Commun.* **2018**, *9*, 2767.
(31) Horcas, I.; Fernández, R.; Gómez-Rodríguez, J. M.; Colchero, J.; Gómez-Herrero, J.; Baro, A. M. WSXM: A Software for Scanning Probe Microscopy and a Tool for Nanotechnology. *Rev. Sci. Instrum.* **2007**, *78*, 013705.
(32) Kresse, G.; Furthmüller, J. Efficient Iterative Schemes for *Ab Initio* Total-Energy Calculations Using a Plane-Wave Basis Set. *Phys. Rev. B* **1996**, *54*, 11169−11186.
(33) Hohenberg, P.; Kohn, W. Inhomogeneous Electron Gas. *Phys. Rev.* **1964**, *136*, B864−B871.
(34) Kohn, W.; Sham, L. J. Self-Consistent Equations Including Exchange and Correlation Effects. *Phys. Rev.* **1965**, *140*, A1133−A1138.
(35) Kresse, G.; Joubert, D. From Ultrasoft Pseudopotentials to the Projector Augmented-Wave Method. *Phys. Rev. B* **1999**, *59*, 1758−1775.
(36) Pack, J. D.; Monkhorst, H. J. Special Points for Brillouin-Zone Integrations. *Phys. Rev. B* **1977**, *16*, 1746−1747.
(37) Wang, V.; Xu, N.; Liu, J. C. VASPKIT: A Pre- and Post-Processing Program for VASP Code. 2020, arXiv:1908.08269 [cond-mat.mtrl-sci]. arXiv.org e-Print archive. https://arxiv.org/abs/1908.08269 (accessed February 22, 2020).

https://dx.doi.org/10.1021/acsnano.0c03149
ACS Nano 2020, 14, 11262−11272